# Size-Selective Incorporation of DNA Nanocages into Nanoporous Antimony-Doped Tin Oxide Materials

**Chad R. Simmons,[†,‡] Dominik Schmitt,[‡,§] Xixi Wei,[†,‡] Dongran Han,[†,‡] Alex M. Volosin,[‡] Danielle M. Ladd,[‡] Dong-Kyun Seo,[‡,*] Yan Liu,[†,‡] and Hao Yan[†,‡,*]**

[†]The Biodesign Institute and [‡]Department of Chemistry and Biochemistry, Arizona State University, Tempe, Arizona 85287, United States. [§]On leave from Inorganic Chemistry Laboratory, Johannes Gutenberg University of Mainz, Mainz, Germany.

**ABSTRACT** A conductive nanoporous antimony-doped tin oxide (ATO) powder has been prepared using the sol–gel method that contains three-dimensionally interconnected pores within the metal oxide and highly tunable pore sizes on the nanoscale. It is demonstrated that these porous materials possess the capability of hosting a tetrahedral-shaped DNA nanostructure of defined dimensions with high affinity. The tunability of pore size enables the porous substrate to selectively absorb the DNA nanostructures into the metal oxide cavities or exclude them from entering the surface layer. Both confocal fluorescence microscopy and solution FRET experiments revealed that the DNA nanostructures maintained their integrity upon the size-selective incorporation into the cavities of the porous materials. As DNA nanostructures can serve as a stable three-dimensional nanoscaffold for the coordination of electron transfer mediators, this work opens up new possibilities of incorporating functionalized DNA architectures as guest molecules to nanoporous conductive metal oxides for applications such as photovoltaics, sensors, and solar fuel cells.

**KEYWORDS:** DNA nanotechnology · DNA nanocages · nanoporous materials · antimony-doped tin oxide (ATO) · conductive metal oxides

Transparent conducting oxides (TCOs)[1,2] with mesoporosity or nanoporosity provide great promise for a variety of purposes due to the highly conductive nature of the material, with potential applications such as optoelectronic chemical sensing or enhancing photon harvesting efficiency in solar fuel cells.[3,4] Porous conductors that contain large cavity networks inside the material significantly increase the surface area accessible to guest molecules, for example, electron transfer mediators, to allow efficient contact with the internal surface of the electrode and to permit mass fluid flow throughout the material.[3,4]

One of the most widely used transparent conducting oxides (TCOs) is indium tin oxide (ITO).[1,2] A drawback of this material is its high cost due to low earth abundance of indium, and thus an alternative is desirable.[5] Recently, the development of antimony-doped tin oxide (ATO) as a conductive electrode surface has emerged as an advantageous alternative to ITO[5] because it is less expensive and significantly more thermally stable, and it has the potential ability to achieve optimal conductivity as a mesoporous electrode.[6] Synthesis of ATO films has been reported for electro-optical applications, and yet challenges still remain in pore size control and pore accessibility.[6]

Among other synthetic methods for mesoporous metal oxides, the hard template method (or nanocasting) has been successful in providing mesoporous networks within various metal oxides that often require high-temperature calcination.[7–9] Specifically, porous carbon templates like carbon aerogels can provide mesoporous materials with three-dimensionally interconnected networks.[8] However, the method can be cumbersome because the carbon templates must be pre-prepared and also the impregnation of the templates needs to be carried out often multiple times to ensure good oxide framework connectivity. To avoid these problems, a new one-pot synthetic method based on sequential formation of interpenetrating metal oxide/polymer composite gels has been developed and successfully applied to produce mesoporous ATO material with controllable pore sizes (unpublished data). Herein, we utilize DNA nanostructures of well-defined dimensions to test the effectiveness of the three-dimensionally interconnected mesopores in the ATO materials to size selectively adsorb guest materials (Figure 1).

DNA has been widely used as a structural material to construct supramolecular nanostructures.[10,11] Its outstanding properties include its simple connectivity, predictable structure, and inter- and intramolecular interactions. Its rigidity can be easily modulated by including regions of single-stranded DNA and crossovers to allow it to form branched structures.[12] In recent years, more researchers have used these principles to design higher order self-assembled

* Address correspondence to hao.yan@asu.edu, dseo@asu.edu.

Received for review May 25, 2011 and accepted June 22, 2011.

**Published online June 22, 2011**
**10.1021/nn2019286**

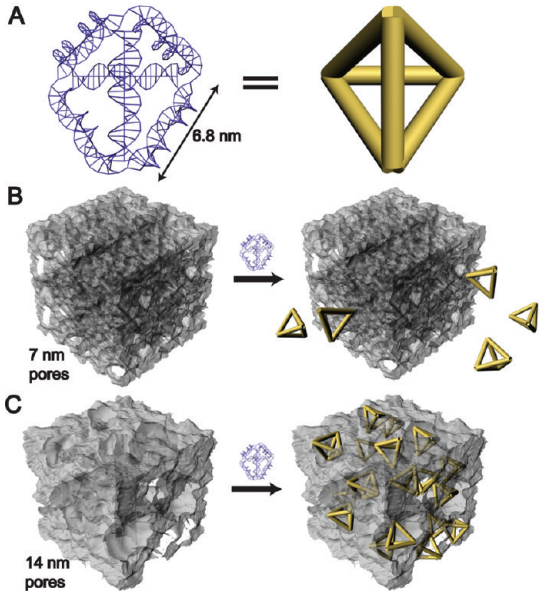


**Figure 1. Experimental scheme of the tetrahedral DNA nanocage structure incubated in the presence of "narrow" and "broad" nanoporous antimony-doped tin oxide (ATO). (A) Indicated is a wire representation of the DNA tetrahedron (left) containing 20 base pairs on each of the helical edges, corresponding to approximately 6.8 nm per side. The DNA represented with the rod-like structure (right) is indicated to represent the tetrahedron in the cartoons below. (B) Shown is a cartoon of the "narrow" porous ATO which contains pores with an average size of ~7 nm (left) which are then incubated in the presence of the DNA nanocage (right). The image demonstrates that the tetrahedron is completely excluded from the narrow pores. (C) Cartoon representation of the "broad" porous ATO containing average pore sizes of ~14 nm (left) incubated in the presence of the DNA structure. The image (right) demonstrates complete uptake of the tetrahedron into the nanopores.**

molecular cages that form rigid "hierarchical" structures, including cubes, prisms, tetrahedra, and other complicated polyhedra.[13−18]

One of the outstanding advantages for DNA nanostructures is their ability to function as scaffolds for the discrete position and orientation of a host of biological or inorganic materials with nanometer precision. DNA is highly programmable, and the nucleotides can undergo many different specific chemical modifications to be further functionalized to template the distance specific interaction of a large number of guest molecules such as peptides,[19] proteins,[20−24] and nanoparticles.[25−29] One example of protein encapsulation within a DNA cage was the covalent conjugation of cytochrome *c* on one component DNA strand, so that the protein can be incorporated into the center cavity of a tetrahedral DNA nanostructure.[30] Green fluorescence protein (GFP) has also been site-specifically linked to DNA using "click" chemistry with four GFP molecules bound per tetrahedron structure.[31]

The construct we have chosen in this report is a self-assembled DNA tetrahedron designed by Turberfield and co-workers[32] consisting of four component oligonucleotides containing complementary regions on each of the other strands (Figure 1A). Each edge contains 20 base pairs that are ~6.8 nm long. Neighboring edges are connected together at each vertex by single-stranded regions, called "hinge" bases.

Herein we demonstrated the size-specific incorporation of intact 3D DNA nanocages into the pores of a conductive nanoporous metal oxide. This allows us to establish the groundwork for new opportunities for loading functionalized DNA nanostructures into conductive nanoporous metal oxides as the host material, maintaining a relatively well-defined local environment for the guest molecules hosted inside the DNA nanocage. This development holds promise for future applications, such as enhancement of catalysis for DNA-conjugated proteins, delivery of light harvesting dyes and nanoparticles, *etc.*, inside the confined conductive porous materials while keeping their structural integrity for their proper function. This capability could then provide advances for fields such as energy storage, chemical sensing, and photoelectronics.

## RESULTS AND DISCUSSION

Conductive porous antimony-doped tin oxide (ATO) materials were prepared using a sol−gel method (unpublished data). The average pore size was measured using $N_2$ adsorption based on the Barrett−Joyner−Halenda (BJH) model, and it was revealed that the average pore size can be controlled by varying the relative concentrations of starting precursor materials (see details in the Methods section). Two different ATO porous materials were obtained, and the ATO with an average pore size of ~14 nm was defined as "broad" and that with an average pore size of ~7 nm as "narrow" (Table S1 in Supporting Information lists the pore size characterization). Porous alumina was also prepared in parallel as described previously,[33] and the average pore diameter was measured to be ~25 nm (Table S1). The DNA tetrahedron was incubated in the presence of both the narrow and broad ATO, and the inclusion or exclusion of the DNA structure was investigated. Figure 1B,C illustrates such processes. The images from scanning electron microscopy (SEM) show relatively smooth surfaces of the materials in microscale (Figure 2A−C). The materials were further characterized by employing scanning transmission electron microscopy (STEM). In the STEM images (Figure 2D−F and Figure S2 in Supporting Information), the porous nature of the materials is clearly visible and the width of the cavities could be measured in high resolution (Figure 2G−I). Although alumina could not be used as a conductive platform for the proposed work, it provided an excellent template upon which we could characterize the affinity of the pores for the tetrahedral DNA nanocage using optical methods.

To demonstrate preferential binding of the DNA tetrahedron to the porous materials, we used fluorescence

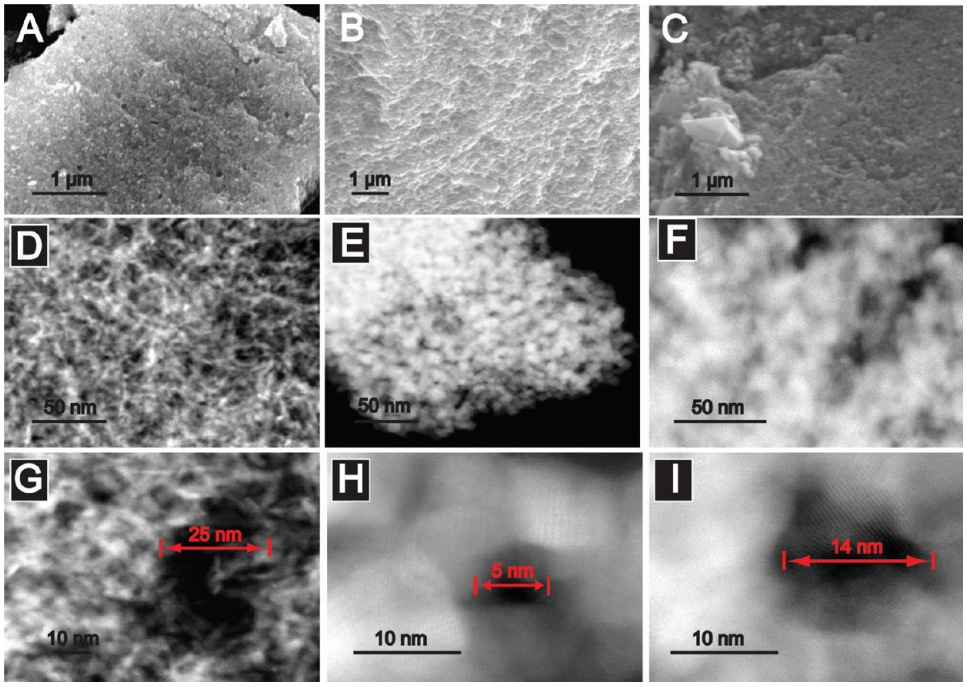


**Figure 2. SEM and STEM images of the nanoporous samples. (A,D,G) Alumina; (B,E,H) narrow ATO; (C,F,I) broad ATO. Scale bars for each image are indicated.**

confocal microscopy to visualize a Cy3-labeled DNA nanocage upon incubation with the three porous materials. Bulk ATO is an opaque material that does not allow efficient penetration of light through it. However, alumina is translucent (Figure 3A and Figure S3), which allows three-dimensional imaging by confocal microscopy. As observed in Figure 3B, the clear solution background and the intense fluorescence signal from the alumina sample demonstrated the preference absorption of Cy3-labeled DNA tetrahedron onto the surface (or into the interior) of the alumina. Due to the low background fluorescent signal in the surrounding solution, we conclude that there is nearly complete uptake of the DNA tetrahedron by the alumina material. In order to distinguish whether the DNA structures were uniformly adsorbed throughout the internal pores of the alumina, or they were only adsorbed on the outer surface of the material, a Z-sectioning of the confocal microscope image was performed. Because alumina is colorless and more transparent, light was allowed to penetrate the entire sample, enabling us to systematically section from the "top" to the "bottom" of the material (Figure S4). A representative Z-slice from approximately the center of the sample is shown in Figure 3C–E, demonstrating distribution of the fluorescent signal from inside the porous matrix. Upon three-dimensional reconstruction of the Z-stacked images, we conclude that DNA nanocages were distributed throughout the entire porous material but not simply interacting with the outer surface (Figure 3F–H).

As previously mentioned, the average pore size is ~7 nm for the narrow ATO and ~14 nm for the broad ATO. Each edge of the six-sided DNA tetrahedron corresponding to a length of ~6.8 nm (Figure 1A–C). The hydrodynamic diameter of the DNA nanocage was determined to be ~9–10 nm by dynamic light scattering. Therefore, the narrow ATO was not expected to uptake the DNA nanostructures into its pores, but the broad ATO should have pore sizes large enough for efficient uptake. Fluorescence confocal microscope images for the narrow porous ATO samples that were incubated with the Cy3-labeled nanocage indeed showed strong fluorescence background outside of the material with no observable uptake of the structure into the pores of the ATO (Figure 4A and Figure S5A), though we cannot rule out the possibility that some DNA nanostructures were adsorbed onto the outer surface. In contrast, the broad ATO particles were able to exclusively absorb all of the dye-labeled nanocages into their pores (Figure 4B and Figure S5B,C), which left a very low fluorescence intensity in the solution background but an intense emission on top of the solid materials, which was similar to the result observed with the alumina sample. These observations indicated that the binding of the structure into the pores is size-specifically excluded from the narrow ATO but becomes very efficient for the broad ATO. Although light in the confocal microscope cannot penetrate the opaque ATO material so that we cannot get the 3D slicing of the sample to give an interior view of the pores, it can be speculated that the pores within the ATO are much like a network of pores that percolates throughout the material, similar to that observed within the alumina material with larger average pore sizes (Figure 3C–H).

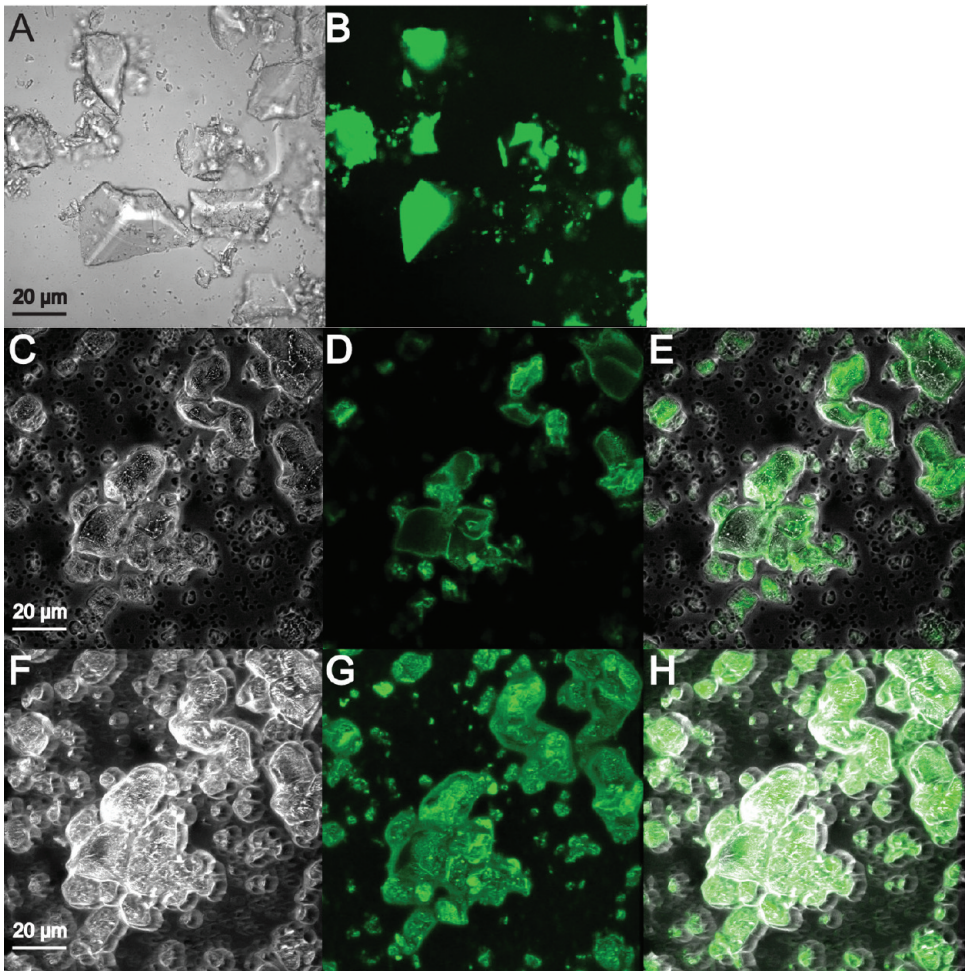


**Figure 3. Confocal images of Cy3-labeled DNA tetrahedra within the pores of alumina. (A) Transmitted image; (B) Cy3 fluorescence image; (C) transmitted light image of a representative Z-section cutting through the middle of the larger particles; (D) Cy3 fluorescence image of the same Z-section; (E) superimposition of images shown in (C) and (D); (F) 3D reconstruction of the Z-sectioned transmitted light images; (G) 3D reconstruction of Z-stacked Cy3 fluorescence images; (H) superimposition of images shown in (F) and (G).**

To address the concerns over whether the tetrahedral DNA nanostructure remains stable upon its binding within the porous pockets, we labeled the 5′ end of another strand of the tetrahedron with a Cy5 dye to form a fluorescence resonance energy transfer (FRET) pair within the tetrahedron, and the donor Cy3 and acceptor Cy5 are at a rough distance of ~3.4 nm. Since the Cy3/Cy5 pair has a Förster radius $R_o$ = 54 Å,[34] efficient FRET is expected if the DNA nanostructure remains intact. The structure containing the FRET pair was annealed, purified, and then incubated in the presence of the porous materials for 24 h, and again the fluorescence confocal microscope was used to observe the fluorescence energy transfer between the FRET pair. Figure 5A and Figure S6A,B demonstrate that, when the dual-label DNA nanostructure was incubated with the porous alumina sample, upon excitation of Cy3 (at 543 nm), it yielded a signal at both the Cy3 emission wavelength (green channel) and the Cy5 emission wavelength (red channel) throughout the material. The fluorescence images superimposed very well (colored yellow). When the DNA nanostructure was incubated with the narrow ATO, the structure was indeed excluded from the pores and the FRET pair remained intact in solution (Figure 5B). Only the surface of the material showed both green and red emissions possibly due to drying of the sample during the imaging, so that the DNA nanostructures were found surrounding the narrow ATO instead of entering the pores (Figure 5B and Figure S7A,B). When the DNA nanostructures were incubated with the broad ATO, complete uptake was observed and similar corresponding green and red fluorescence emissions were observed inside the material (Figure 5C and Figure S8A,B). Since the superimposed images showed constant yellow color, we believe the DNA tetrahedron structure remained intact when it was absorbed inside the pores of the material. Lambda scans of the resulting fluorescence images within the material showed similar intensity ratios for the Cy3/Cy5 emissions as that for the solution sample, which confirmed the observed confocal FRET signal (data not shown).

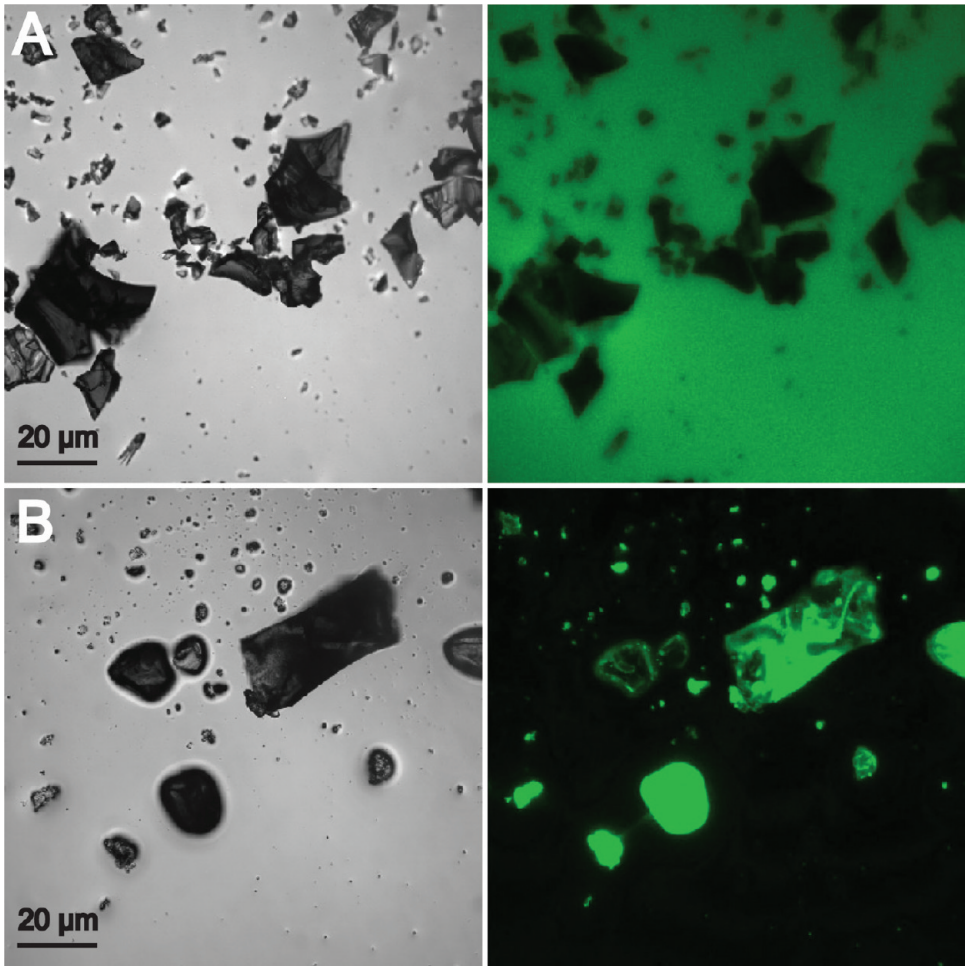


**Figure 4. Confocal imaging of nanoporous broad and narrow ATO incubated with Cy3-labeled DNA tetrahedra. (A) Narrow ATO. Left and right, transmitted light image and Cy3 fluorescence image. (B) Broad ATO. Left and right, transmitted light image and Cy3 fluorescence image. Note the contrast difference of the fluorescence intensities on the background and on top of the material for the two samples.**

We also analyzed uptake of the DNA tetrahedron into the porous materials by monitoring the remaining fluorescent signal in the supernatant solution after centrifugation to remove the porous material after 24 h of incubation. We anticipated that after removal of the porous material, if the uptake was efficient as in the alumina and the broad ATO, there would be a greatly reduced fluorescent signal in the remaining solution compared to the solution before incubation. Each of the incubations were performed using the same experimental conditions for the confocal experiments, with the equivalent concentration of the DNA structure (1 $\mu$M in 110 $\mu$L) and approximately $\sim$50 $\mu$g of the solid porous material. The amount of the porous material used was calculated to have a total surface area to be able to absorb all of the DNA nanostructures added to the solution at near saturation level. Figure 6 compares the control (red) sample containing DNA tetrahedron in the absence of porous material to the supernatant samples after incubation with different porous materials. The fluorescence profile of the solution after incubation with the narrow ATO yielded a FRET signal that was very similar to the control sample, indicating <12% loss of the DNA nanostructure after the incubation, possibly due to some adsorption of the DNA nanocage to the outer surface of the narrow pore material, consistent to that shown in Figure 5B. By contrast, the sample after incubation with alumina and broad ATO displayed 92% and 85% reduction of the fluorescent signal, respectively, which clearly revealed that the DNA nanocages had been absorbed efficiently by these porous materials.

Our ultimate goal is to form maximal surface contacts of the conductive porous material with an electrode to minimize loss of electronic signal and, at the same time, to minimize loss of the light that illuminates the guest molecules inside the porous material; this can be achieved by making a thin layer of conductive porous material supported on a transparent electrode. Toward this goal, we had synthesized transparent ATO with porous matrices of tunable sizes on glass cover slides to optimize conditions for hosting the guest DNA nanocage. The confocal microscope images shown in Figure 7 clearly demonstrated the homogeneous surface of the conductive porous ATO on the glass cover

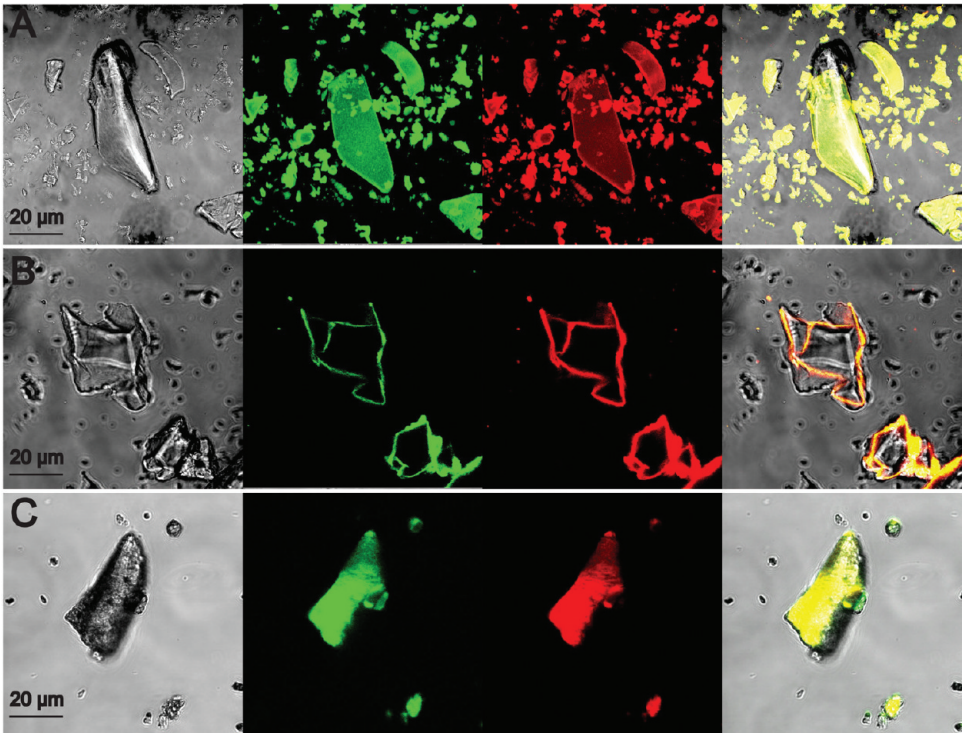


**Figure 5. Confocal imaging of the three nanoporous materials incubated with the Cy3/Cy5 dual-labeled DNA tetrahedron. (A) Alumina. (B) Narrow ATO. (C) Broad ATO. Four images in each row, from left to right, are the transmitted light image, Cy3 emission image, Cy5 emission image (both under Cy3 excitation), and superimposition of the three left images.**

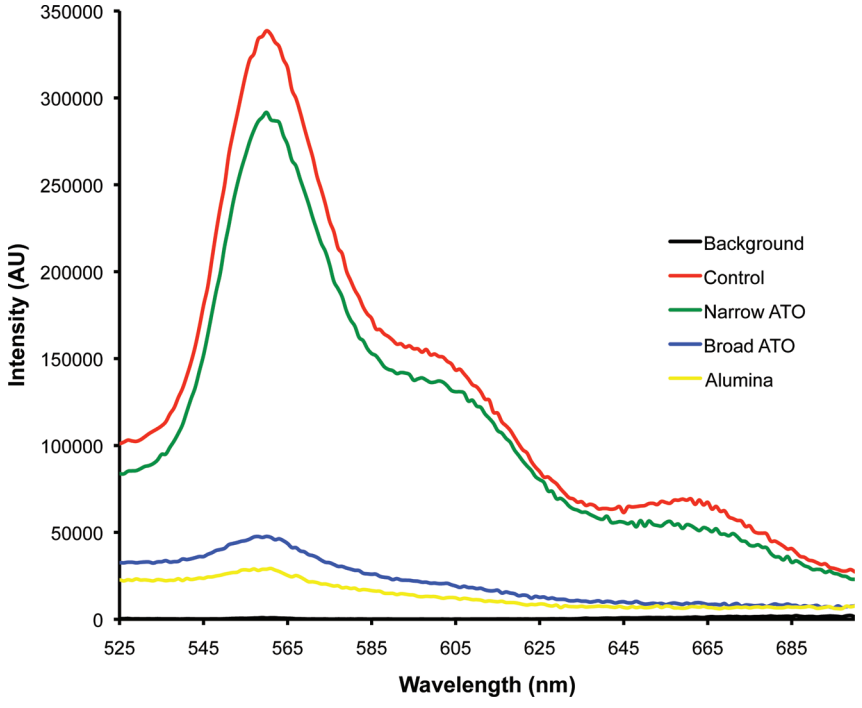


**Figure 6. Cy3/Cy5 emission spectra of supernatant solutions after incubation of the dual-labeled DNA tetrahedra with the nanoporous materials. Red trace is the control solution containing only the Cy3/Cy5 dual-labeled DNA nanostructure without incubation with any material. Green, blue, and yellow traces are the spectra of supernatant solution after incubation with narrow ATO, broad ATO, and alumina, respectively. Black trace is the background (buffer solution). Fluorescence emission scan was performed from 525 to 700 nm with excitation wavelength at 460 nm.**

slides, which showed efficient uptake of the FRET-labeled DNA nanostructure. Work is currently underway to optimize these conditions and use different transparent conductive materials as substrates (and electrodes)

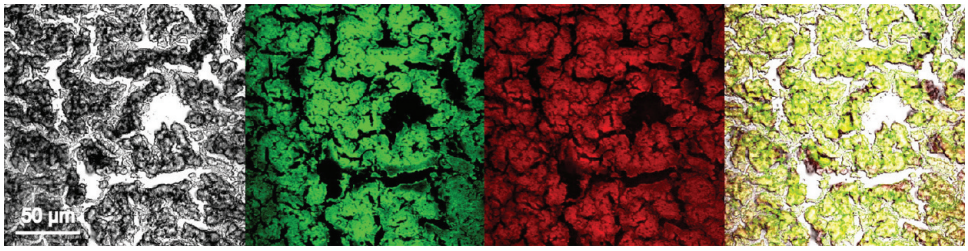


**Figure 7. Confocal images for the Cy3/Cy5 dual-labeled DNA tetrahedra incubated with broad ATO coated on glass cover slides. From left to right are the transmitted light image, Cy3 emission image; Cy5 emission image; and superimposition of the three images.**

to support these porous materials, which will be reported elsewhere.

## CONCLUSIONS AND PERSPECTIVES

Both fluorescence microscope imaging and solution spectroscopy results have demonstrated that the DNA nanostructure can be absorbed within pores of sizes larger than its own lateral size and remain stable. However, the DNA nanostructures are completely excluded from materials with smaller average pore sizes. The size-specific and nondestructive uptake of a functionalized (loaded) DNA nanocage into a porous conductive material is advantageous for electrochemical applications because it overcomes many of the typical hurdles that are encountered when macromolecules are directly attached to electrodes, including lack of solubility and denaturation. Although the FRET experiment suggests that the structure remains as an intact complex within the metal oxide material, we cannot rule out the possibility that the bound tetrahedral structure may be somehow distorted upon interaction with the porous surface. It has been shown that DNA nanostructures, when deposited onto silica surfaces,[35] still maintain structural integrity. We expect the porous materials described here will not cause severe damage to the 3D DNA cage structure, while this needs to be further investigated in future studies. Achievement of electrodes that possess optical transparency and electrical conductivity with large internal surface area within the matrix make the nanoporous material well-suited for hosting various functional molecules for the development of light emitting diodes, photoelectrochemical devices, chemical sensors, and water splitting solar fuel cells.

## METHODS

**Porous Material Fabrication.** The preparation of the porous alumina followed a previously published method.[33] The detailed synthesis of the bulk nanoporous ATO materials will be published separately with physical property characterizations (unpublished data). In a typical synthesis, the materials were prepared by dissolution of stoichiometric amounts of $SbCl_3$ (Alfa Aesar, Ward Hill, MA) and $SnCl_4 \cdot 5H_2O$ (Sigma-Aldrich, St. Louis, MO) in a ~1:1 mixture of absolute ethanol (Decon, King of Prussia, PA) and deionized water, followed by addition of designated amounts of resorcinol (Sigma-Aldrich) and 37% formaldehyde solution (Sigma-Aldrich) (resorcinol/formaldehyde = 0.5). The molar concentration of the Sn precursor was fixed at 0.4 M (6 atom % Sb). The concentrations of resorcinol were 0.23 M for the narrow ATO and 0.45 M for the broad ATO material, as they provided average pore sizes of ~7 and ~14 nm, respectively. The resorcinol/formaldehyde concentration ratio was fixed at 1:2.

The precursor solution mixture was then placed in an ice bath for 10 min with magnetic stirring. Then, propylene oxide (PO, Alfa Aesar) was added slowly to the precursor solution chilled in an ice bath, while stirring, to give a 0.8 M PO concentration. After the solution was removed from the ice bath, a translucent light yellow gel formed in about a minute. The gel was aged at room temperature for 24 h, yielding an opaque red/orange gel surrounded with a residual transparent yellow liquid. Then, the resulting material was placed in an oven (Yamato DKN 400) at 70 °C for 5 days, which resulted in a hardened, opaque reddish brown monolith surrounded by a residual clear, light yellow liquid. The monolith was broken into approximately 1 $cm^3$ pieces, dried in air at room temperature for 24 h, and calcined in an ashing furnace (Thermolyne 48000) for 10 h at 500 °C. Finally a low-density, dark blue particle with measurable conductance was produced.

For the coating of ATO on glass coverslips, the entire procedure was essentially the same, except that polyethylene glycol (PEG, MW 17 500) was added into the metal precursor solution before the resorcinol and formaldehyde were added. The amount of PEG was 13% of the total weight of the final precursor solution. The viscous solution was then spread onto a glass coverslip using the doctor-blade method. The films were then placed in closed containers at room temperature for 24 h, followed by heating in an oven at 70 °C for 3 days. The films were then heated in a box furnace at 500 °C for 10 h to yield a homogeneous translucent layer of ATO with a relatively uniform thickness of ~400 nm supported on the glass slips. Multiple replicates of the samples were prepared for different analyses.

**SEM and STEM Imaging.** Approximately 10 $\mu$g of bulk alumina holder.and broad and narrow ATO samples was washed by nanopure water. The samples were transferred to an SEM stub containing conductive tape and aluminum foil, allowed to dry, and then the surface was sputter coated with gold colloid. Images were collected on a FEI/Philips XL30 field emission gun environmental scanning electron microscope at an acceleration voltage of 20 kV, a spot size of 5, and at a working distance of 11 mm. Size analysis for each image was performed using the XL30 software (scale bars are indicated on each image). High-resolution high angle annular dark field scanning transmission electron microscopy (HAADF-STEM) was performed on a JEOL JEM 2010F electron microscope operating at 200 kV using ultrathin carbon-coated 400 mesh copper grids as the sample substrates.

**DNA Sequence Design and Purification.** The DNA sequences used in the assembly of the tetrahedron are equivalent to those first used by Turberfield and colleagues.[32] All DNA strands were ordered from Integrated DNA Technologies (IDT, Coralville, IA), including modified strands 1 and 4 (Supporting Information) that were labeled with Cy3 or Cy5 on the 5′ ends, respectively. Both dye-labeled strands were HPLC purified by IDT, and the other unmodified DNA strands were purified by electrophoresis using 8% denaturing PAGE gels. Corresponding bands were visualized with ethidium bromide, excised from the gel, incubated at room temperature in standard elution buffer (500 mM ammonium acetate, 10 mM magnesium acetate, and 1 mM EDTA) overnight, and the ethidium stain was removed from the extracted DNA using *n*-butanol, and the purified DNA was subsequently ethanol precipitated and resuspended in water. The concentrations were quantified *via* measuring absorbance at 260 nm and then adjusted to 100 $\mu$M.

**DNA Tetrahedron Annealing and Purification.** Stoichiometric ratios of all four strands were mixed to a final concentration of 200 nM. The total volume of the annealing reaction for a typical preparation was 10 mL in 1× TAE $Mg^{2+}$ buffer (40 mM Tris base, 20 mM acetic acid, 2 mM EDTA·$Na_2$·$12H_2O$, 12.5 mM Mg $(CH_3COO)_2 \cdot 4H_2O$). The sample was heated to 95 °C and immediately cooled on ice to 4 °C. The annealing reaction was then concentrated to ~500 $\mu$L in a 15 mL Amicon concentrator (Billerica, MA) and applied at 1 mL/min to a HiLoad 16/60 Superdex S200 Prep grade size exclusion column (GE Healthcare, Piscataway, NJ), with 1× TAE $Mg^{2+}$ buffer as the mobile phase. The resulting monomeric tetrahedron peak fractions were then collected, pooled, and concentrated to a final concentration of ~5 $\mu$M as determined by $A_{260}$.

**Sample Preparation and Confocal Imaging.** Ten microliters of a 1 $\mu$M solution of dye-labeled tetrahedron was incubated at room temperature in the presence of 50 $\mu$g of porous alumina or broad or narrow ATO overnight on a sealed cap over 500 $\mu$L of 1× TAE $Mg^{2+}$ buffer. Here the hanging drop vapor diffusion method was used to prevent the samples from drying (Qiagen, Valencia, CA). The samples for imaging were removed as a 5 $\mu$L suspension with a pipet from the incubation drop and deposited on a 22 × 60 mm micro cover glass. All fluorescent images were collected through a Plan-Neoflur 40×/1.3 oil DIC at a working distance of 0.17 using a Zeiss LSM 510 laser scanning microscope (Carl Zeiss, Gottingen, Germany) connected to a LSM510 laser module with the following lasers: HeNe543 (Cy3-green channel), HeNe633 (transmitted light image for the Cy3 only fluorescence images), and the diode 405-50 was used for the transmitted light images for the Cy3/Cy5 FRET confocal imaging experiments. The Cy5 (red channel) was recorded with the module set to 657-711. Fluorescence was recorded as square 8-bit images (512 × 512 pixels). Pixel time for imaging was generally 1.6 $\mu$s, with a scan speed of ~8 s per image section, using line mode. Z-sections were recorded, and then Z-stacked images were reconstructed and projected using the Zeiss LSM software.

**Solution FRET Measurements.** A quantity of 110 $\mu$L of 1 $\mu$M Cy3/Cy5-labeled tetrahedron solution was incubated with ~50 $\mu$g of each of the porous materials at room temperature overnight by gently shaking on a vortexer tube holder. The samples were centrifuged at 10 000 rpm for 5 min, then the supernatant was removed and the fluorescence emission spectra from 525 to 700 nm were measured at room temperature in a quartz cell with 1 cm path length on a NanoLog spectrometer (HORIBA Jobin Yvon, equipped with a thermoelectric cooled PMT) using 560 nm excitation wavelength.

*Acknowledgment.* We thank Z. Deng for technical help in STEM imaging. This work was supported by the Center for Bio-Inspired Solar Fuel Production, an Energy Frontier Research Center funded by the U.S. Department of Energy, Office of Science, Office of Basic Energy Sciences under Award Number DE-SC0001016.

*Supporting Information Available:* Statistical analysis of the porous materials, DNA sequences, DNA tetrahedron characterization, additional STEM and confocal images. This material is available free of charge *via* the Internet at http://pubs.acs.org.

## REFERENCES AND NOTES

1. Ginley, D. S.; Bright, C. Transparent Conducting Oxides. *MRS Bull.* **2000**, *25*, 15–18.
2. Lewis, B. G.; Paine, D. C. Applications and Processing of Transparent Conducting Oxides. *MRS Bull.* **2000**, *25*, 22.
3. Emons, T. T.; Li, J.; Nazar, L. F. Synthesis and Characterization of Mesoporous Indium Tin Oxide Possessing an Electronically Conductive Framework. *J. Am. Chem. Soc.* **2002**, *124*, 8516–8517.
4. Mbarek, H.; Saadoun, M.; Bessais, B. Screen-Printed Tin-Doped Indium Oxide (ITO) Films for $NH_3$ Gas Sensing. *Mater. Sci. Eng., C* **2006**, *26*, 500–504.
5. Gordon, G. R. Criteria for Choosing Transparent Conductors. *MRS Bull.* **2000**, *25*, 52–57.
6. Hou, K.; Puzzo, D.; Helander, M. G.; Lo, S. S.; Bonifacio, L. D.; Wang, W.; Lu, Z.-H.; Scholes, G. D.; Ozin, G. A. Dye-Anchored Mesoporous Antimony-Doped Tin Oxide Electrochemiluminescence Cell. *Adv. Mater.* **2009**, *21*, 2492–2496.
7. Schüth, F. Endo- and Exotemplating to Create High-Surface Area Inorganic Materials. *Angew. Chem., Int. Ed.* **2003**, *42*, 3604–3622.
8. Li, W.-C.; Lu, A.-H.; Schmidt, W.; Schüth, F. High Surface Area, Mesoporous, Glassy Alumina with a Controllable Pore Size by Nanocasting from Carbon Aerogels. *Chem.—Eur. J.* **2005**, *11*, 1658–1664.
9. Zhang, Z.; Zuo, F.; Feng, P. Hard Template Synthesis of Crystalline Mesoporous Anatase $TiO_2$ for Photocatalytic Hydrogen Evolution. *J. Mater. Chem.* **2010**, *20*, 2206–2212.
10. Seeman, N. C. DNA in a Material World. *Nature* **2003**, *421*, 427–431.
11. Lin, C.; Liu, Y.; Yan, H. Designer DNA Nanoarchitectures. *Biochemistry* **2009**, *48*, 1663–1674.
12. Seeman, N. C.; Lukeman, P. S. Nucleic Acid Nanostructures: Bottom-Up Control of Geometry on the Nanoscale. *Rep. Prog. Phys.* **2005**, *68*, 237–270.
13. Chen, J.; Seeman, N. C. Synthesis from DNA of a Molecule with the Connectivity of a Cube. *Nature* **1991**, *350*, 631–633.
14. Zhang, Y.; Seeman, N. C. Construction of a DNA-Truncated Octahedron. *J. Am. Chem. Soc.* **1994**, *116*, 1661–1669.
15. He, Y.; Ye, T.; Su, M.; Zhang, C.; Ribbe, A. E.; Jiang, W.; Mao, C. Hierarchical Self-Assembly of DNA into Symmetric Supramolecular Polyhedra. *Nature* **2008**, *452*, 198–202.
16. Zhang, C.; Su, M.; He, Y.; Zhao, X.; Fang, P.; Ribbe, A. E.; Jiang, W.; Mao, C. Conformational Flexibility Facilitates Self-Assembly of Complex DNA Nanostructures. *Proc. Natl. Acad. Sci. U.S.A.* **2008**, *105*, 10665–10669.
17. Yang, H.; McLaughlin, C. K.; Aldaye, F. A.; Hamblin, G. D.; Rys, A. Z.; Rouiller, I.; Sleiman, H. F. Metal–Nucleic Acid Cages. *Nat. Chem.* **2009**, *1*, 390–396.
18. Aldaye, F. A.; Sleiman, H. F. Modular Access to Structurally Switchable 3D Discrete DNA Assemblies. *J. Am. Chem. Soc.* **2007**, *129*, 13376–13377.
19. Williams, B. A.; Lund, K.; Liu, Y.; Yan, H.; Chaput, J. C. Self-Assembled Peptide Nanoarrays: An Approach To Studying Protein–Protein Interactions. *Angew. Chem., Int. Ed.* **2007**, *46*, 3051–3054.
20. Yan, H.; Park, S. H.; Finkelstein, G.; Reif, J. H.; LaBean, T. H. DNA Templated Self-Assembly of Protein Arrays and Highly Conductive Nanowires. *Science* **2003**, *301*, 1882–1884.
21. Park, S. H.; Yin, P.; Liu, Y.; Reif, J. H.; LaBean, T. H.; Yan, H. Programmable DNA Self-Assemblies for Nanoscale Organization of Ligands and Proteins. *Nano Lett.* **2005**, *5*, 729–733.
22. Voigt, N. V.; Tørring, T.; Rotaru, A.; Jacobsen, M. F.; Ravnsbæk, J. B.; Subramani, R.; Mamdouh, W.; Kjems, J.; Mokhir, A.; Basenbacher, F.; Gothelf, K. V. Single Molecule Chemical Reactions on DNA Origami. *Nat. Nanotechnol.* **2010**, *5*, 200–203.
23. Chhabra, R.; Sharma, J.; Ke, Y.; Liu, Y.; Rinker, S.; Lindsay, S.; Yan, H. Spatially Addressable Multiprotein Nanoarrays

Templated by Aptamer-Tagged DNA Nanoarchitectures. *J. Am. Chem. Soc.* **2007**, *129*, 10304–10305.
24. Rinker, S.; Ke, Y.; Liu, Y.; Chhabra, R.; Yan, H. Self-Assembled DNA Nanostructures for Distance-Dependent Multivalent Ligand−Protein Binding. *Nat. Nanotechnol.* **2008**, *3*, 418–422.
25. Le, J. D.; Pinto, Y.; Seeman, N. C.; Musier-Forsyth, K.; Taton, T. A.; Kiehl, R. A. DNA-Templated Self-Assembly of Metallic Nanocomponent Arrays on a Surface. *Nano Lett.* **2004**, *4*, 2343–2347.
26. Sharma, J.; Chabra, R.; Liu, Y.; Ke, Y.; Yan, H. DNA-Templated Self-Assembly of Two-Dimensional and Periodical Gold Nanoparticle Arrays. *Angew. Chem., Int. Ed.* **2006**, *45*, 730–735.
27. Zhang, J.; Liu, Y.; Ke, Y.; Yan, H. Periodic Square-like Gold Nanoparticle Arrays Templated by Self-Assembled Two-Dimensional DNA Nanogrids on a Surface. *Nano Lett.* **2006**, *6*, 248–251.
28. Zheng, J.; Constantinou, P. E.; Micheel, C.; Alivisatos, A. P.; Kiehl, P. A.; Seeman, N. C. 2D Nanoparticle Arrays Show the Organizational Power of Robust DNA Motifs. *Nano Lett.* **2006**, *6*, 1502–1504.
29. Sharma, J.; Chhabra, R.; Cheng, A.; Brownell, J.; Liu, Y.; Yan, H. Control of Self-Assembly of DNA Tubules through Integration of Gold Nanoparticles. *Science* **2009**, *323*, 112–116.
30. Erben, C. M.; Goodman, R. P.; Turberfield, A. J. Single-Molecule Protein Encapsulation in a Rigid DNA Cage. *Angew. Chem., Int. Ed.* **2006**, *45*, 7414–7417.
31. Duckworth, B. P.; Chen, Y.; Wollack, J. W.; Sham, Y.; Mueller, J. D.; Taton, T. A.; Distefano, M. D. A Universal Method for the Preparation of Covalent Protein−DNA Conjugates for Use in Creating Protein Nanostructures. *Angew. Chem., Int. Ed.* **2007**, *46*, 8819–8822.
32. Goodman, R. P.; Schaap, I. A. T.; Tardin, C. F.; Erben, C. M.; Berry, R. M.; Schmidt, C. F.; Turberfield, A. J. Rapid Chiral Assembly of Rigid DNA Building Blocks for Molecular Nanofabrication. *Science* **2005**, *310*, 1661–1665.
33. Ladd, D. M.; Volosin, A.; Seo, D.-K. Preparation of Highly Porous $\gamma$-Alumina *via* Combustion of Biorenewable Oil. *J. Mater. Chem.* **2010**, *20*, 5923–5929.
34. Ha, T.; Rasnik, I.; Cheng, W.; Babcock, H. P.; Gauss, G. H.; Lohman, T. M.; Chu, S. Initiation and Re-initiation of DNA Unwinding by the *Escherichia coli* Rep Helicase. *Nature* **2002**, *419*, 638–641.
35. Kershner, R. J.; Bozano, L. D.; Micheel, C. M.; Hung, A. H.; Fornof, A. R.; Cha, J. N.; Rettner, C. T.; Bersani, M.; Frommer, J.; Rothemund, P. W. K.; *et al.* Placement and Orientation of Individual DNA Shapes on Lithographically Patterned Surfaces. *Nat. Nanotechnol.* **2009**, *3*, 557–561.